[INVITED] Improved parameters for the lanthanide $4f^q$ and $4f^{q-1}5d$ curves in HRBE and VRBE schemes that takes the nephelauxetic effect into account

Dorenbos, Pieter

DOI
10.1016/j.jlumin.2020.117164

Publication date
2020

Document Version
Final published version

Published in
Journal of Luminescence

Citation (APA)
Dorenbos, P. (2020). [INVITED] Improved parameters for the lanthanide $4f^q$ and $4f^{q-1}5d$ curves in HRBE and VRBE schemes that takes the nephelauxetic effect into account. *Journal of Luminescence*, *222*, Article 117164. https://doi.org/10.1016/j.jlumin.2020.117164

Journal of Luminescence 222 (2020) 117164

Contents lists available at ScienceDirect

Journal of Luminescence

journal homepage: www.elsevier.com/locate/jlumin

Full Length Article

[INVITED] Improved parameters for the lanthanide $4f^q$ and $4f^{q-1}5d$ curves in HRBE and VRBE schemes that takes the nephelauxetic effect into account

Pieter Dorenbos

Delft University of Technology, Faculty of Applied Sciences, Department of Radiation Science and Technology, Section Luminescence Materials, Mekelweg 15, 2629 JB Delft, Netherlands

A B S T R A C T

In first approximation the binding of an electron in lanthanide $4f^q$ ground states changes with q in a characteristic zigzag shape that is independent on type of compound. Those shapes have been parameterized in past publications and are used to construct host referred binding energy (HRBE) or vacuum referred binding energy (VRBE) schemes showing the lanthanide $4f^q$ level locations with respect to the host valence bands or to the vacuum level. There is experimental evidence for a slight compound dependence, and a model explaining that has appeared recently (Dorenbos, 2019). This all implies that the parameters for constructing HRBE and VRBE schemes need to be revised and a compound dependence needs to be introduced as a second order approximation. In this work the improved parameters are derived from the 3^{rd} and 4^{th} ionization potentials of the lanthanide atoms. In compounds, as explained by the chemical shift model, the free ion binding energy curves undergo an upward shift due to Coulomb repulsion from anion ligands and they undergo a tilt due to the lanthanide contraction. In this work we will use the nephelauxetic parameter β to add a compound dependence. Its main effect is an increased binding in the $4f^q$ ground states for the lanthanides from the right hand branch (q > 7) of the zigzag curves. The same applies for the $4f^{q-1}5d$ excited states with $(q-1) > 7$. Collected spectroscopic data on divalent and trivalent lanthanides from more than 1000 different compounds have been analyzed to arrive at the proposed revised parameters for the $4f^q$ and $4f^{q-1}5d$ binding energy curves.

1. Introduction

The binding energy of an electron in the lanthanide $4f^q$ (q = 1–14) and $4f^{q-1}5d$ states with respect to that in the host bands in inorganic materials, but equally well in solutions, metals, or organic materials, follows very systematic and therefore predictable patterns with increasing q [1–3]. It has led to predictive models on the energy of 4f–5d transitions [4,5], 5d crystal field splitting [6–9] and 5d centroid shift [10], on where to locate the lanthanide levels within the band gap and how to construct so-called host referred binding energy (HRBE) [11] and vacuum referred binding energy (VRBE) diagrams [12,13]. These models and diagrams are now well-established [14–16], confirmed with ab-initio calculations [17–21], and frequently used for interpretation of data and for predicting [22–25], and to some extent, engineering of properties [26].

The models require information from experiment to pin at least one lanthanide ground state within the band gap and to establish the lowest 4f–5d transition energy for one lanthanide. Usually data for Eu^{2+} and Ce^{3+} serve that purpose. Once pinned, those of all other lanthanides can be generated from the systematics. The systematics itself is based on collecting and analyzing a vast amount of spectroscopic data over the years. Fig. 1 shows the VRBE diagram for the lanthanides in YPO_4 constructed with the latest 2017 parameters from [27]. The shapes of the divalent and trivalent zigzag curves are always treated to be independent on type of compound. However, evidence from thermoluminescence and thermobleaching experiments indicate that (1) the shape of the trivalent zigzag curve needs to be reconsidered [28], (2) the shape, particularly that for the right hand branch of the zigzag curves, shows a slight dependence on type of compound. The entire right hand branch may lower several 0.1 eV with respect to the left hand branch due to the nephelauxetic effect, i.e. due to a dependence of the 4f interelectron repulsion on type of compound [29].

There is an unexplained feature in the 'old style' HRBE and VRBE diagrams when comparing the lowest energy $4f^{q-1}5d$ excited states of YPO_4 with that of for example $La_2Hf_2O_7$ in Fig. 2. For the $4f^{q-1}5d$ levels, a distinction is made between the high spin [HS] $4f^{q-1}5d$ states and the higher energy (if $q > 7$) low spin [LS]$4f^{q-1}5d$ states. In the [HS] state, the 5d electron has spin parallel to the total spin in the $4f^{q-1}$ orbital and in the [LS] state it is anti-parallel. It leads to two branches of the $4f^{q-1}5d$ curve [30]. Those for $q > 7$ can be seen in Fig. 1 for YPO_4 and in Fig. 2 for $La_2Hf_2O_7$. The energy difference or exchange splitting $\Delta E^{exc}(q, 3+, A)$ between both branches decreases when q increases from 8 to 14 [30]. Splitting also depends on type of compound and is relatively large in YPO_4 but 30% smaller in $La_2Hf_2O_7$. In HRBE and VRBE scheme construction, the [LS] and [HS] 5d levels for $q > 7$ behave in an unexplained fashion. This is illustrated in Fig. 2 where two [HS] branches are shown. The dashed one with open data

E-mail address: p.dorenbos@tudelft.nl.

https://doi.org/10.1016/j.jlumin.2020.117164
Received 11 December 2019; Received in revised form 1 February 2020; Accepted 23 February 2020
Available online 27 February 2020

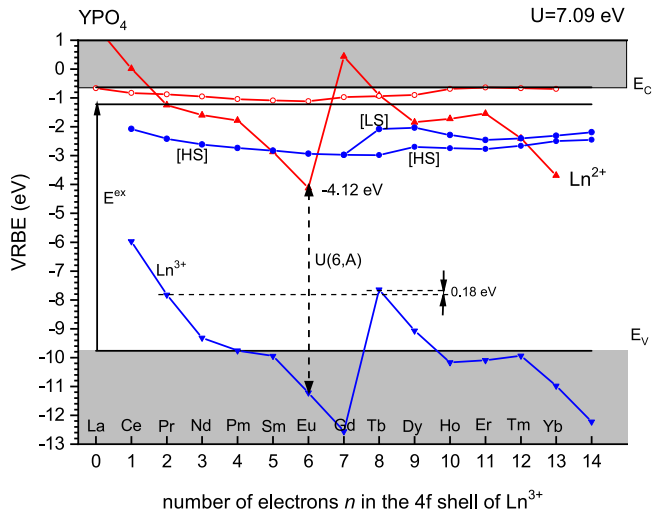

Fig. 1. The vacuum referred binding energy scheme for the divalent and trivalent $4f^q$ lanthanide ground state levels and lowest energy $4f^{q-1}5d$ excited state levels in YPO_4 constructed with the 2017 parameters from [27].

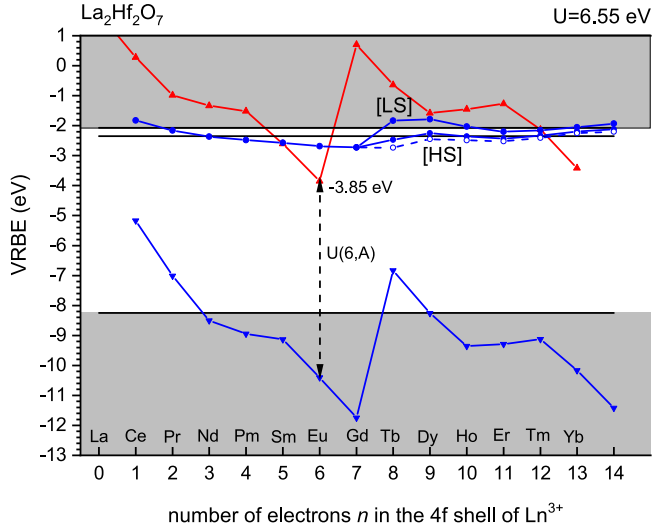

Fig. 2. The vacuum referred binding energy scheme for the divalent and trivalent $4f^q$ lanthanide ground state levels and $4f^{q-1}5d$ excited state levels in $La_2Hf_2O_7$ constructed with the 2017 parameters from [27]. The dashed [HS] branch with open data symbols is obtained when using the exchange splitting valid for YPO_4.

symbols is obtained by assuming the same values for exchange splitting as for YPO_4, and the one with solid data symbols represents the actual situation for $La_2Hf_2O_7$. The reduced exchange splitting raises the [HS] branch but does not seem to affect the [LS] branch. However, the lowest $4f^{q-1}5d$ levels for the lanthanides with $q < 8$ have also [HS] character and should be raised similarly. As it is now a kink appears between $q = 7$ and $q = 8$ in the [HS] level energies as function of q. By implementing the nephelauxetic effect, this kink will disappear and instead of raising the [HS] levels for $q > 7$ the higher energy [LS] levels are lowered. This work will provide an explanation and a more correct method for HRBE and VRBE scheme construction.

A new set of parameters for the divalent and trivalent zigzag curves of $4f^q$ ground state energies and the lowest energy [HS] and [LS] $4f^{q-1}5d$ excited states will be defined in this work. First, data on the energy of valence band (VB) to Ln^{3+} electron transfer will be combined with data from thermo-luminescence (TL) and thermo-bleaching studies (TB) to demonstrate that the $4f^q$ curve is compound dependent. That compound dependence has only significant effect for the right

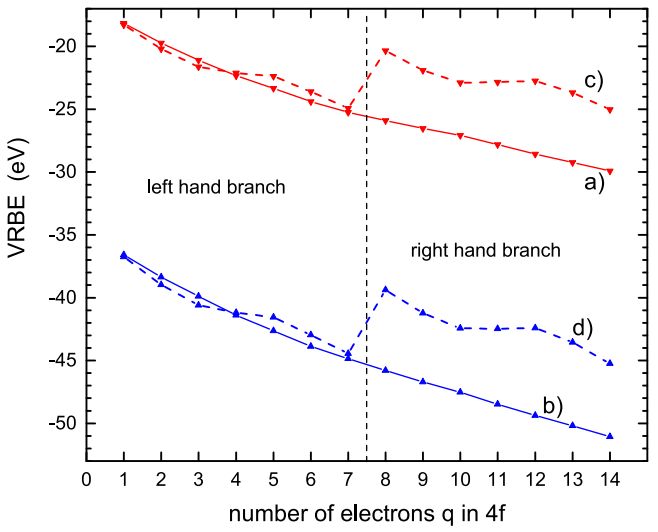

Fig. 3. The smooth functions (a) $C(q, 2+)$ and (b) $C(q, 3+)$ for the free lanthanide ions in vacuum. Adding the $S(q, Q)$ functions provides the free ion VRBE in the $4f^q$ ground states for (c) the divalent lanthanides and (d) the trivalent lanthanides.

hand branch of the zigzag curve, and the effect will be accounted for by the nephelauxetic ratio $\beta(Q, A)$. Next, the revised parameters to obtain the $4f^{q-1}5d$ curves need to be determined. For that we will add information on the $4f^q$-$4f^{q-1}5d$ energy differences using the well-established systematics in [4] from the year 2000. In that work a set of parameters was defined for the lowest energy $4f^q \rightarrow 4f^{q-1}5d$ transitions in, what was called, the quasi free trivalent lanthanides. In compounds these energies are lowered for each lanthanide by the same amount known as the redshift $D(3+, A)$ [5,31]. Later the same was established for the divalent lanthanides [5,32]. More data is now available and an update is provided on those quasi free lanthanide parameters. The size of the exchange splitting $\Delta E^{exc}(q, Q, A)$ and the value for $\beta(Q, A)$ appear to be correlated, and we will show that the rise of the [HS] $4f^{q-1}5d$ levels of e.g. $La_2Hf_2O_7$ caused by a reduced ΔE^{exc} is not entirely correct. Due to the nephelauxetic effect the right hand branch of the $4f^q$ levels is lowered by few 0.1 eV which when taking into account compensates for the rising [HS] curve.

2. The lanthanide $4f^q$ zigzag curves

The VRBE $E_{4f}(q, Q, A)$ in the $4f^q$ ground state of the lanthanide with charge Q in chemical environment A is given by the following equation from [29]

$$E_{4f}(q, Q, A) = C(q, Q) + \beta(Q, A)S(q, Q) + E(Eu, Q, A) + \alpha(Q)(R(Eu, Q) - R(q, Q)) \quad (1)$$

where $C(q, Q)$ represents the binding of a 4f-electron to the nucleus together with the repulsion from the electrons of the [Xe] configuration of the lanthanide cation. $S(q, Q)$ is the contribution to the binding energy from the Coulomb repulsion between 4f-electrons as derived from the spin pairing theory of Jørgensen [33,34]. The values for C and S as established in [29] are compiled in Table 1 for the divalent and in Table 2 for the trivalent lanthanides. $C(q, Q)$ are smoothly varying functions with q and shown as curves (a) and (b) in Fig. 3. The $S(q, Q)$ functions show an oscillating pattern for q is 1–7, and for q is 8–14, and there appears a 5–6 eV step which separates the left hand branch lanthanides from the right hand branch ones. The sum of $C(q, Q)$ and $S(q, Q)$ is equal to the VRBE in the free lanthanide $4f^q$ ground state levels and gives the characteristic zigzag curves (c) and (d) in Fig. 3. $\beta(Q, A)$ is the nephelauxetic ratio defined below in Eq. (2). $E(Eu, Q, A)$ is the chemical shift for the 4f ground state of

Table 1
The parameters required to establish the divalent lanthanide $4f^q$ and $4f^{q-1}5d$ level energies in compounds. tilt(2+) accounts for the contribution of the lanthanide contraction to the binding energy as calculated with $\alpha(2+) = 0.095$ eV/pm and the lanthanide ionic radii (pm) in column 3. All energies are in eV.

q	Ln^{2+}	$R(q,2+)$	$C(q,2+)$	$S(q,2+)$	tilt(2+)	$E_{fd}^{SA}(q,2+)$	$\Delta E^{exc}(q,2+)$
1	La	148.7	−18.170	−0.116	−0.90	−0.89	–
2	Ce	147.0	−19.723	−0.475	−0.73	0.41	–
3	Pr	145.3	−21.087	−0.537	−0.58	1.59	–
4	Nd	143.7	−22.325	0.223	−0.42	1.90	–
5	Pm	142.2	−23.331	0.962	−0.28	1.94	–
6	Sm	140.7	−24.390	0.789	−0.13	3.00	–
7	Eu	139.3	−25.249	0.329	0.00	4.20	0.00
8	Gd	137.9	−25.901	5.566	0.13	0.60	0.84
9	Tb	136.6	−26.535	4.625	0.25	1.85	0.60
10	Dy	135.4	−27.084	4.194	0.36	2.55	0.40
11	Ho	134.3	−27.809	4.969	0.47	2.49	0.33
12	Er	133.2	−28.569	5.829	0.58	2.35	0.28
13	Tm	132.2	−29.243	5.563	0.67	3.08	0.21
14	Yb	131.3	−29.913	4.883	0.761	4.38	0.19

Table 2
The parameters required to establish the trivalent lanthanide $4f^q$ and $4f^{q-1}5d$ level energies in compounds. tilt(3+) accounts for the contribution of the lanthanide contraction to the binding energy as calculated with $\alpha(3+) = 0.098$ eV/pm and the lanthanide ionic radii (pm) in column 3. All energies are in eV.

q	Ln^{3+}	$R(q,3+)$	$C(q,3+)$	$S(q,3+)$	tilt(3+)	$E_{fd}^{SA}(q,3+)$	$\Delta E^{exc}(q,3+)$
1	Ce	128.3	−36.591	−0.167	−0.76	6.17	–
2	Pr	126.6	−38.370	−0.610	−0.59	7.68	–
3	Nd	125.0	−39.895	−0.705	−0.44	8.95	–
4	Pm	123.4	−41.387	0.187	−0.28	9.26	–
5	Sm	121.9	−42.627	1.072	−0.14	9.40	–
6	Eu	120.5	−43.870	0.900	0.00	10.46	–
7	Gd	119.2	−44.852	0.402	0.13	11.77	0.00
8	Tb	117.9	−45.792	6.422	0.26	7.81	1.00
9	Dy	116.7	−46.712	5.487	0.38	9.33	0.88
10	Ho	115.6	−47.524	5.089	0.49	10.02	0.42
11	Er	114.5	−48.478	5.998	0.59	9.92	0.32
12	Tm	113.5	−49.375	6.955	0.69	9.84	0.28
13	Yb	112.5	−50.191	6.631	0.79	10.93	0.22
14	Lu	111.7	−51.066	5.816	0.86	12.24	0.17

Eu^Q due to the Coulomb repulsion from the surrounding anion ligands in the chemical environment A. The last term in Eq. (1) accounts for the chemical shift differences of lanthanides with respect to that for Eu due to the lanthanide contraction. $R(Eu,Q)$ and $R(q,Q)$ are the lanthanide ionic radii. The values compiled in Tables 1 and 2 are from [35] and based on the Shannon ionic radii for the lanthanides on 8-fold coordinated sites [36]. Those for the divalent lanthanides are taken 18.7 pm larger than those for the trivalent ones. $\alpha(Q)$ are the tilt parameters in eV/pm. For the lanthanides in vacuum $\beta = 1$, $\alpha = 0$, and $E(Eu,Q,A) = 0$. This work will assume that the tilt parameters are compound independent, and we will find that $\alpha(2+) = 0.095$ eV/pm and $\alpha(3+) = 0.098$ eV/pm provide results consistent with available experimental data. Columns 6 in Tables 1 and 2 show that the tilt raises the VRBE for the smallest lanthanides Yb^{2+} and Lu^{3+} by about 0.8 eV and lowers that of the large La^{2+} and Ce^{3+} by about 0.8 eV.

It may be that $C(q,Q)$ is somewhat different in a chemical environment A but it is expected that it remains a smooth function of q. Its effect is then in first approximation incorporated in the value chosen for the tilt parameter $\alpha(Q)$. The nephelauxetic ratio $\beta(Q,A)$ was introduced as a parameter to characterize the reduction of the 4f-interelectron repulsion when lanthanides are in a chemical environment. The repulsion can be expressed by the Slater Condon parameters $F^k(k = 0,2,4,6)$ that can be derived experimentally from fitting the energies of all excited state $^{2S+1}L_J$ multiplets by means of crystal field theory. F^0 is not of relevance. F^2 is the most important, and since the values for F^4 and F^6 show constant ratio's with that of F^2 [37] one may define the ratio [29]

$$\beta(q,Q,A) \equiv \frac{F^2(q,Q,A)}{F^2(q,Q,\text{vacuum})} \tag{2}$$

as a measure for the reduction of interelectron repulsion in a chemical environment. Other measures for the effect have appeared in literature. Caro and Derouet [38] for example defined for Nd^{3+}, $\beta(3,3+,A)$ as the average of the ratio between the energy of the excited $4f^3$ levels in compound A with that in LaF_3. β is foremost a compound property and in this work we will ignore a dependence on q and simply write $\beta(Q,A)$. Tanner and Yeung [39] collected data on the F^k parameters for Pr^{3+} in many different compounds, and from that work $\beta(3+,A)$ is about 0.96 for fluoride compounds, 0.94 for oxides with strongly bonded oxygen ligands as in sulphates and phosphates. It steadily decreases from borates to silicates to aluminates until typical values of 0.92 for La_2O_3. For the sulfides and selenides it may further decrease towards 0.9. For the divalent lanthanides, $\beta(2+,A)$ behaves similarly with type of compound although one may not exclude a systematic difference with $\beta(3+,A)$.

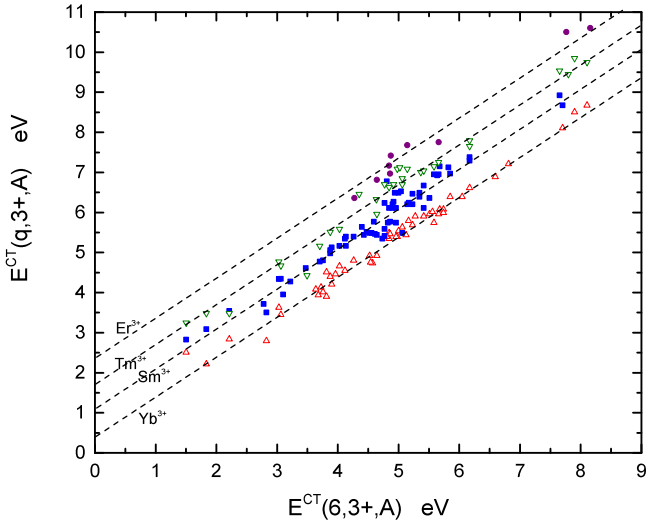

Fig. 4. The energy $E^{CT}(q,3+,A)$ of the CT-bands for trivalent Yb ($q = 13$, open up-triangle data points), Sm ($q = 5$, square data points), Tm ($q = 12$, open down-triangle data points), and Er ($q = 11$, bullet data points) against that of Eu^{3+} ($q = 6$). Dashed lines are least squares fits with unit slope.

2.1. The divalent lanthanide zigzag curve

To arrive at a representation for the $4f^q$ zigzag curves, we will use Eq. (1) where the values for α and β are to be determined from available experimental data. One approach is based on the energy needed to transfer an electron from the top of the valence band to a trivalent lanthanide like Eu^{3+}, Yb^{3+}, Sm^{3+}, Er^{3+}, or Tm^{3+}. It provides information on the location of the corresponding divalent lanthanide ground state levels above the valence band top in the band gap. The approach was introduced in 2003 in [11]. In that work already much data and references were compiled, but since then more data have become available which motivated to repeat the entire procedure in this work. Data are most abundant for Eu^{3+} and information on 635 different compounds has been gathered. Fig. 4 shows the CT-energies for trivalent Yb, Sm, Tm, Er against that of Eu^{3+} when in the same compound. A similar figure for other lanthanides (Nd, Dy, Ho) can be found in Fig. S1 [Suppl. Info.] Data distribute around the drawn dashed lines with unit slope evidencing that the energy differences between lanthanide ground states in the bandgap are fairly fixed and to first approximation independent on type of compound. $\Delta E^{CT}(q,6)$ is defined as

$$\Delta E^{CT}(q,6) = \overline{E^{CT}(q,3+,A) - E^{CT}(6,3+,A)} \tag{3}$$

Table 3
The compound averaged energy difference $\Delta E^{CT}(q,6)$ between the VB→Ln^{3+} CT-energy for Ln^{3+} that has $4f^q$ ground state with that for Eu^{3+} ($q = 6$). N is the number of compounds and σ_{sd} the standard deviation. Energies are in eV.

q	Ln	$\Delta E^{CT}(q,6)$	σ_{sd}	N
3	Nd	2.28	–	1
5	Sm	1.12	0.25	65
6	Eu	0.00	–	635
9	Dy	2.16	0.25	15
10	Ho	2.38	0.04	2
11	Er	2.34	0.24	9
12	Tm	1.67	0.24	28
13	Yb	0.44	0.18	51

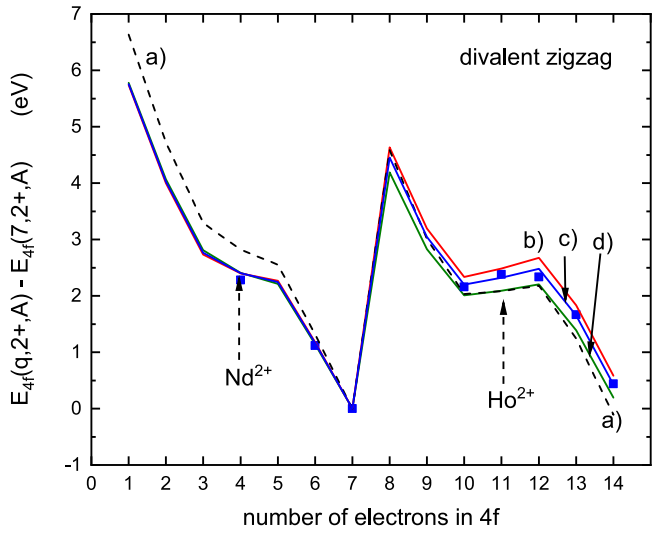

Fig. 5. The $4f^q$ zigzag curve for the divalent lanthanides relative to the energy $E_{4f}(7,2+,A)$ of the Eu^{2+} ground state. Dashed curve (a) shows the $4f^q$ curve for the free divalent lanthanides. (b), (c), and (d) are obtained using a tilt factor of $\alpha(2+) = 0.095$ eV/pm. (b) reflects the situation for BaF_2 with $\beta(2+,A) = 0.985$, (c) for YPO_4 with $\beta(2+,A) = 0.95$, and (d) for compounds with $\beta(2+,A) = 0.90$. The eight square solid data points are from energies of VB→ Ln^{3+} electron transfer band energies.

where the average is made over the number of compounds A information is available on. The $\Delta E^{CT}(q,6)$ values, the number of compounds information is available on, and standard deviations are compiled in Table 3.

Fig. 4 and the standard deviations in Table 3 demonstrate that data tend to scatter quite substantially around the straight lines with unit slope. One reason is the often limited accuracy of up to ±0.2 eV in the CT data, but another is a compound to compound variation in the difference $E^{CT}(q,3+,A) - E^{CT}(6,3+,A)$.

The $\Delta E^{CT}(q,6)$ for the trivalent lanthanides are assumed to be equivalent to $E_{4f}(q,2+,A) - E_{4f}(7,2+,A)$ of the divalent lanthanides. The available values are the eight square data symbols in Fig. 5, and they form already part of the skeleton of the zigzag curve for the 14 divalent lanthanides in compounds. Curve (a) is the same as curve (c) in Fig. 3, and curves (b), (c), and (d) are obtained after applying Eq. (1) with a tilt factor of $\alpha(2+) = 0.095$ eV/pm and different $\beta(2+,A)$ values. In [29] the existence of a nephelauxetic effect on the VRBE in the lanthanide ground state was evidenced by means of thermoluminescence data on lanthanide doped oxides and thermobleaching data on lanthanide doped fluorides. According to Eq. (1), the nephelauxetic effect, and therefore reduced $\beta(2+,A)$ lowers the $S(q,2+)$ contribution to the VRBE. When $\beta(2+,A)$ reduces from 0.985, 0.95, to 0.90 the left hand branch energies are not altered significantly but the entire right hand branch energies can be lowered by almost 0.5 eV. This is illustrated by curves (b), (c), and (d) in Fig. 5.

A most accurate method to probe the shape of the divalent zigzag curve is by means of thermo-luminescence (TL) spectroscopy, and the most complete data set is available for the YPO_4:Ce^{3+};Ln^{3+} system. Ce^{3+} acts as a very stable and deep hole trapping center and Pr, Nd, Sm, Dy, Ho, Er, Tm, and Yb act as electron trapping centers with trap depths that follow the shape of the divalent zigzag curve. In TL-experiments, after charging the sample, the temperature of the sample is increased at a rate β K/s. The release rate of an electron from the divalent lanthanide grows according to Boltzmann statistics exponentially with temperature, and the moment it can escape to the conduction band it will recombine with the hole trapped on Ce to generate characteristic Ce^{3+} 5d–4f emission. A glow peak is observed reaching maximum intensity at temperature T_m that is to good approximation proportional to the trap depth [40]. When trap depths are derived from VRBE schemes as in Fig. 1, several 0.1 eV error in the energy E_C at the conduction band bottom will lead to a systematic error in the derived trap depths. Then, instead of the theoretical proportional relation, we expect to observe a linear relation between trap depths read from VRBE diagrams and the T_m from glow peaks.

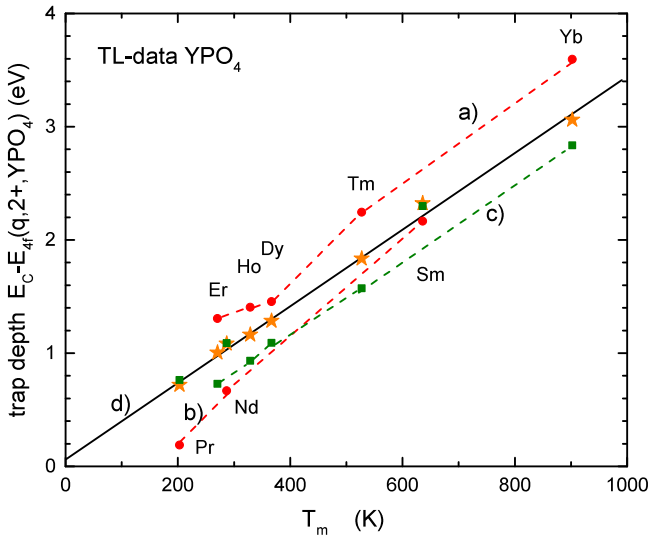

Fig. 6. The electron trapping depth in the divalent lanthanides against the temperature T_m of the glow peak maximum in TL-spectra of YPO_4:Ce^{3+};Ln^{3+} at heating rate of 0.1 K/s. The bullet data points on curves (a) and (b) are obtained when the free ion zigzag curve is used to derive trapping depths, the square data points on curves (c) and (d) are obtained when a zigzag curve with $\alpha(2+) = 0.095$ eV/pm and $\beta(2+,A) = 1.0$ is used, the star data points on curve (d) are obtained when a zigzag curve with $\alpha(2+) = 0.095$ eV/pm and $\beta(2+,A) = 0.95$ is used. Curves (a) and (c) connect data for lanthanides from the right hand branch and curve (b) from the left hand branch.

For YPO_4 in Fig. 1, the bottom of the conduction band is at $E_C = -0.63$ eV and the Eu^{2+} ground state is located at −4.12 eV. If the free ion divalent zigzag curve (c) (in Fig. 3) is pinned at −4.12 eV for Eu^{2+}, then how deep each trivalent lanthanide will trap an electron can be read from the diagram. The bullet shaped data points in Fig. 6 show the thus obtained electron trapping depth against the glow peak temperature T_m in YPO_4 as obtained from Bos et al. [41,42]. The data from the right hand branch lanthanides connected by curve (a) for Er, Ho, Dy, Tm, and Yb indeed follow a linear relation. The same applies to the data of Pr, Nd, Sm from the left hand branch connected by dashed curve (b). However, both branches taken together do not follow the same linear relation. Therefore, the shape of the free ion zigzag curve is not consistent with the TL trapping data. We knew that already because of the lanthanide contraction that causes a tilt of the free ion curve. By using Eq. (1) with a tilt factor of $\alpha(2+) = 0.095$ eV/pm and $\beta(2+,A) = 1$ a revised zigzag curve can be pinned at −4.12 eV and another set of trapping depths are obtained. Now, the left hand branch data for Pr, Nd, and Sm are close to the solid line (d) but those of the right hand branch connected by curve (c) have moved below. Apparently, we still have not a proper representation of the binding energy curve. Next we

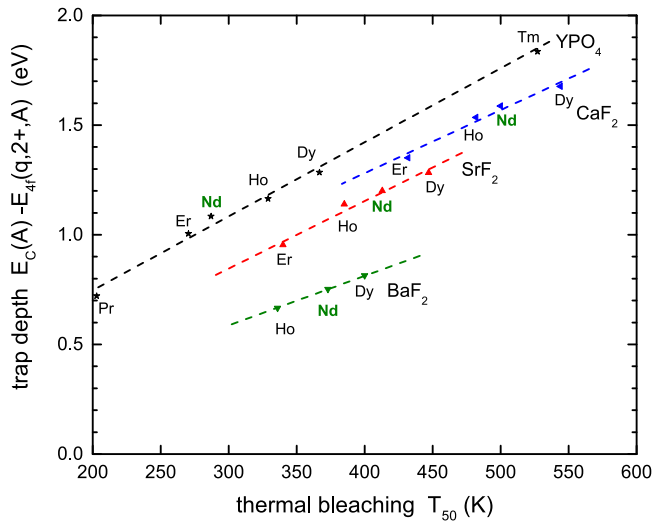

Fig. 7. The electron trapping depth against the thermal bleaching T_{50} temperature of Ln^{2+} absorption in Ba-, Sr-, and CaF_2. The trapping depths in the Ln^{2+} ground states below the conduction band bottom E_C were obtained with $\alpha(2+) = 0.095$ eV/pm and $\beta(2+, A)$ values of 0.985, 0.98, 0.978 for Ba-, Sr-, and CaF_2. For comparison trapping depths in YPO_4 obtained with $\alpha(2+) = 0.095$ eV/pm and $\beta(2+, A) = 0.95$ against the TL glow peak maximum T_m are shown. Dashed lines are from linear fits.

add the nephelauxetic effect by lowering $\beta(2+, A)$ in Eq. (1) from 1.00 to 0.95 to obtain zigzag curve (c) in Fig. 5. Again a new set of trapping depths are obtained and now, when displaced against T_m in Fig. 6, all data fall close to the solid line (d) with slope 0.00337 eV/K (297 K/eV) and intercept at 0.077 eV. The intercept value should be regarded as a systematic error in the derived trap depths. Note that zigzag curve (c) in Fig. 5, that applies to YPO_4, is fully consistent with the skeleton of data derived from CT energies.

Fig. 7 shows data from thermal bleaching studies on CaF_2:Sm^{2+};Ln^{3+} and SrF_2:Sm^{2+};Ln^{3+} from [43] and on BaF_2:Yb^{2+};Ln^{3+} from [44] where Sm^{2+} and Yb^{2+} act as electron donor defects and the Ln^{3+} as electron acceptor defects. Photo-induced electron transfer from the donor to the acceptor creates absorption bands due to the formed divalent lanthanides. During heating of the sample, the bleaching of the absorption bands can be monitored and one may determine the temperature T_{50} where absorption intensity is reduced by 50%. Like for TL, one expects a linear relation between T_{50} and the trap depth of the electron in Ln^{2+} [44]. We therefore need to establish the values for $\alpha(2+)$ and $\beta(2+, A)$ in Eq. (1) such that linearity is obtained. Here we assume, as first approximation, the tilt factor $\alpha(2+)$ as compound independent, and then the value of 0.095 eV/pm as found for YPO_4 applies. Constructed VRBE schemes provide E_C of −0.244 eV, −0.635 eV, −1.11 eV and $E_{4f}(7, 2+, A)$ of −4.229 eV, −4.234 eV, and −4.263 eV for CaF_2, SrF_2, and BaF_2, respectively. The obtained trapping depths for $\beta(2+, A)$, values of 0.985, 0.98, 0.978 for Ba-, Sr-, and CaF_2 then appear to provide good consistency, i.e., the data fall close to straight lines in Fig. 7. The intercept values are then respectively −0.11 eV, −0.07 eV, and +0.10 eV and slopes of 0.00237, 0.00305, 0.00293 eV/K or 422, 328, 342 K/eV are obtained. The trapping depths in YPO_4 from TL-data in Fig. 6 have been added to Fig. 7 for comparison. The effect of β reduction is nicely demonstrated by comparing the position of the Nd^{2+} data point from the left hand branch with that of Dy^{2+}, Ho^{2+}, and Er^{2+} from the right hand branch. In BaF_2 the Nd data point is closest to that of Dy^{2+}, it moves towards that of Ho^{2+} in going to SrF_2 and it moves further for CaF_2. For YPO_4 the Nd data point has passed the Ho data point and has moved close to Er^{2+}. It is all related to the nephelauxetic lowering of the right hand branch as illustrated in Fig. 5 where curve (b) with $\beta = 0.985$ represents the shape of the zigzag curve in BaF_2. The entire right hand branch of the zigzag curve moves downward with lowering of β in the sequence BaF_2, SrF_2, CaF_2 and YPO_4. For comparison also the divalent zigzag curve for $\beta(2+, A) = 0.90$ is shown as curve (d) in Fig. 5. It represents the situation in sulfides and selenide compounds where the nephelauxetic effect is largest. One may then predict that in those compounds the Nd data point will move well beyond that of Er.

Table 4
Temperature T_m in K at the maximum of the glow peak for hole release from Pr^{4+} and Tb^{4+} in compounds. $\Delta E(8, 2, A)$ is the estimated energy difference $E_{4f}(8, 3+, A) - E_{4f}(2, 3+, A)$ in eV. The heating rate was 2 K/s for $Y_3Al_5O_{12}$ and 1 K/s for all other compounds. The released hole recombines with the electron trapped at the listed recombination center (RC). $\beta(3+, A)$ is the derived nephelauxetic parameter with $\alpha(3+) = 0.098$ eV/pm.

Compound A	$T_m(Pr^{4+})$	$T_m(Tb^{4+})$	$\Delta E(8, 2, A)$	$\beta(3+, A)$	RC	Ref.
$LaPO_4$	210	240	0.09	0.95	Eu^{3+}	[49,50]
$GdPO_4$	265	280	0.04	0.94	Eu^{3+}	[51]
$LuPO_4$	514	519	0.01	0.94	Bi^{3+}	[49,50]
	–	551	–	–	Yb^{3+}	[49,50]
YPO_4	483	485	0.00	0.94	Bi^{3+}	[49,50]
	490	495	0.01	0.94	Sm^{3+}	[49,50]
	497	507	0.03	0.94	Eu^{3+}	[49,50]
	516	–	–	–	Yb^{3+}	[49,50]
$LiYSiO_4$	568	577	0.03	0.94	Eu^{3+}	[52]
$LiLuSiO_4$	611	614	0.01	0.94	Eu^{3+}	[52]
$Y_3Al_5O_{12}$	590	578	−0.03	0.93	Eu^{3+}	[53]
$GdAlO_3$	428	416	−0.03	0.93	Eu^{3+}	[54]

2.2. The trivalent lanthanide zigzag curve

The shape of the trivalent zigzag curve has always been less well established than that of the divalent one. In principle one can, like for the divalent lanthanides, use the energy for electron transfer from the top of the valence band to a tetravalent lanthanide as basis to reconstruct that shape. However, in oxides usually only the ground states of Ce^{3+}, Pr^{3+} and Tb^{3+} are located within the band gap, see e.g. Figs. 1 and 2. They are also fairly close to the VB-top which implies that the tetra-valent state is difficult to stabilize and CT transitions to Pr^{4+} and Tb^{4+} are in the red or infra-red region. Useful data is only available for Ce^{4+} [45], but with data on only one lanthanide one cannot reconstruct an entire shape.

In [28] it was shown that data can be obtained from the spectroscopy of electron transfer from the Pr^{3+} ground state and Tb^{3+} ground state to the conduction band. These transitions appear as so-called IVCT bands in excitation and absorption spectra [46–48]. Based on about 40 oxide compounds it was found that

$$E_{4f}(8, 3+, A) = E_{4f}(2, 3+, A) - 0.06 \pm 0.11 \text{ eV} \quad (4)$$

which means that the Tb^{3+} ground state is on average close to that of Pr^{3+}. This disagrees with the trivalent zigzag shape based on the 2017 parameters and used for Figs. 1 and 2 where the ground state of Tb^{3+} is at 0.18 eV higher energy.

It was also shown in [28] that a hole in the valence band can be trapped by Pr^{3+} or Tb^{3+} to form Pr^{4+} or Tb^{4+}, and hole release to the valence band can then be probed by thermoluminescence spectroscopy. The temperatures T_m of glow peaks identified to be caused by hole release from Pr^{4+} and Tb^{4+} are compiled in Table 4. In most cases the hole recombines with an electron trapped on a second dopant Eu^{3+} to generate Eu^{3+} emission. For $LuPO_4$ and YPO_4, the Table also compiles T_m values when Bi^{3+}, Sm^{3+} or Yb^{3+} acts as deep electron trap and recombination center. By using the typical rate of 350 K/eV for the shift of T_m with changing drap depth (see also Fig. 7), the difference in T_m between Tb and Pr has been converted into the energy difference $\Delta E(8, 2, A)$ shown in column 4. In the sequence phosphate, silicate, aluminate that difference moves from +0.09 eV towards −0.03 eV. It means that the Tb^{3+} ground state VRBE is within ±0.1 eV the same as that of Pr^{3+} which is in accordance with Eq. (4). It also demonstrates

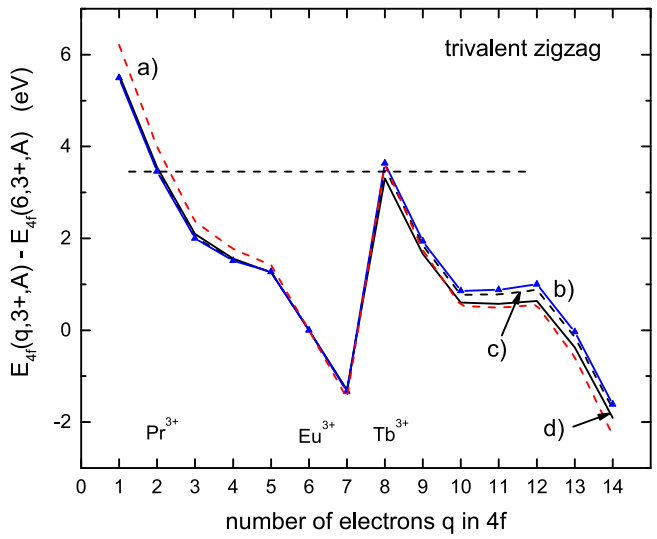

Fig. 8. The $4f^q$ zigzag curve for the trivalent lanthanides relative to the energy $E_{4f}(6,3+,A)$ of the Eu^{3+} ground state. Dashed curve (a) shows the $4f^q$ curve for the free trivalent lanthanides. (b), (c), and (d) are obtained using a tilt factor of $\alpha(2+) = 0.098$ eV/pm. (b) reflects the situation for fluoride compounds with $\beta(3+,A) = 0.96$, (c) for YPO_4 with $\beta(3+,A) = 0.94$, and (d) for compounds with $\beta(3+,A) = 0.90$.

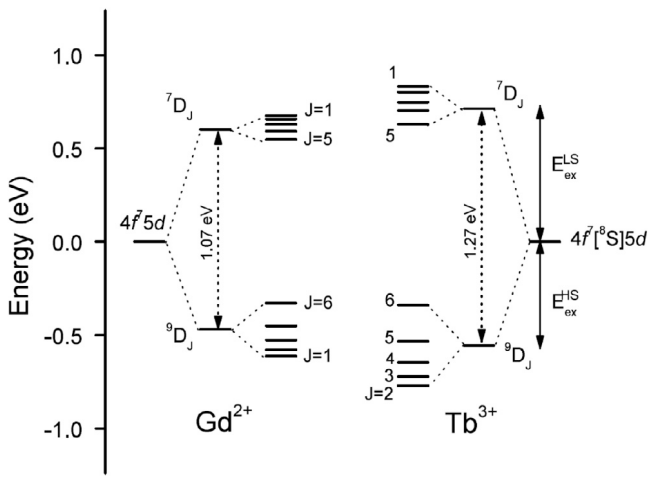

Fig. 9. The effect of exchange splitting on the $4f^7[^8S_{7/2}]5d_1$ levels of the free Gd^{2+} and Tb^{3+} lanthanides.

that with increasing nephelauxetic effect, the Tb^{3+} ground state from the right hand branch moves down by ≈0.12 eV with respect to the Pr^{3+} ground state from the left hand branch.

Note that the type of co-dopant that acts as deep electron trap and recombination center also affects the T_m values quite substantially. The T_m for Pr^{4+} hole release in YPO_4 shifts from 483 K for Bi^{3+} with ionic radius 131 pm, to 490 K for Sm^{3+} (122pm), to 497 K for Eu^{3+} (120 pm) to 516 K for Yb^{3+} (112 pm) suggesting a relation with the ionic radius of the recombination center. At this stage we do not yet know whether recombination proceeds via hole release through the valence band, hole transport via a so-called V_k or trapped hole-center, or whether we deal with a more localized effect where electron trap and recombination center are relatively close neighbors. One does expect that with smaller sized co-dopants the lattice parameter will shrink slightly and this usually leads to band gap widening with lower E_V and higher E_C. A lowering of E_V by about 0.1 eV might explain the observation. Clearly, this topic requires and deserves a separate investigation. Anyway, this all demonstrates the very high sensitivity of the glow peak maximum T_m, and in order to obtain reliable energy differences between Tb^{4+} and Pr^{4+} from glow peak temperatures, the recombination center should be kept the same and also the dopant concentrations.

Taking, like for the divalent zigzag curve, YPO_4 as our reference compound, we wish to apply Eq. (1) with $\beta(3+,YPO_4) = 0.94$ as known from Pr^{3+} 4f–4f spectroscopy [29,39]. $\alpha(3+)$ needs then to be chosen such that the VRBE in the Tb^{3+} $4f^8$ ground state is about 0.01–0.03 eV less than that in the Pr^{3+} $4f^2$ ground state. The desired result is obtained for $\alpha(3+) = 0.098$ eV/pm, and the $4f^q$ curve is shown as curve (c) in Fig. 8. Next, with this value for $\alpha(3+)$ one may determine the value for $\beta(3+,A)$ in order to reproduce the derived energy differences between the Pr^{3+} and Tb^{3+} $4f^q$ ground states. The results are shown in column 5 of Table 4. In the sequence phosphate, silicate, and aluminate it is known from lanthanide spectroscopy that the nephelauxetic effect increases and that $\beta(3+,A)$ decreases accordingly. The derived $\beta(3+,A)$ in Table 4 indeed decreases in that sequence. Moreover, also quantitatively the decrease is the same as derived from spectroscopy. The effect of reduced β value is further illustrated in Fig. 8 which compares the $4f^q$ zigzag curves using $\alpha(3+) = 0.098$ eV/pm and β equal 0.96, 0.94, and 0.90.

3. The energies in the lowest 4f5d levels

Based on the free lanthanide ionization potentials, lanthanide ionic radii and Jørgensen spin pairing theory, Eq. (1) was derived. Experimental information from lanthanide 4f–4f spectroscopy, CT-data, thermoluminescence and thermobleaching then provides the values for the nephelauxetic parameters β and tilt parameters α. It has led to a new representation for the shape of the $4f^q$ zigzag curves of the divalent and trivalent lanthanide ground state energies. The shape is a tilted version of the free ion VRBEs with a lowering of the right hand branch depending on the size of the nephelauxetic ratio β. The divalent lanthanide curve is then pinned in the band gap, usually via the experimentally known $E^{CT}(6,3+,A)$ for Eu^{3+}. By using the $U(6,A)$ value from the chemical shift model, see Fig. 1, the trivalent lanthanide curve is pinned also, and everything is pinned with respect to the vacuum level. Next, one may add the lowest energy $4f^{q-1}5d$ excited states.

For the lowest energy excited $4f^{q-1}5d$-levels a distinction is made between the high spin [HS] and the low spin [LS] $4f^{q-1}5d$ states. This is illustrated for free Gd^{2+} and Tb^{3+} in Fig. 9. On exciting the $4f^8[^7F_6]$ ground state to the $4f^7[^8S_{7/2}]5d_1$ levels, the spin of the electron in $5d_1$ can be parallel or anti-parallel to the total spin of the 7 remaining electrons in 4f. It leads to [HS] ^9D_J levels and [LS] ^7D_J levels separated by the exchange splitting $\Delta E^{exc}(8,Q)$. The size of the exchange splitting vanishes towards the beginning and end of the lanthanide series because of vanishing spin in the lowest state of the $4f^{q-1}$ part of $4f^{q-1}5d$. The size is also dependent on type of compound. The free ion Tb^{3+} value of 1.27 eV reduces to about 1 eV in highly ionic fluorides and to values as low as 0.5 eV in highly covalent compounds [30]. The spin forbidden transitions from the $4f^q$ ground state to the [LS] $4f^{q-1}5d$ excited state for $q < 8$ are always obscured in absorption or excitation spectra by the much more intense spin allowed transitions. However, the spin forbidden transitions to the [HS] $4f^{q-1}5d$ excited states for $q > 7$ can be observed because they appear at lower energy than the first strong spin allowed transition to the [LS] 5d state. In the following we will provide the parameters and methods to construct the [LS] and [HS] 5d branches for $q > 7$ as in Figs. 1 and 2.

3.1. The parameters to construct the 5d level locations for trivalent lanthanides

For trivalent lanthanides a review was made in 2000 on the difference $\Delta E_{fd}^{abs}(q,1,3+)$ between the energy $E_{fd}(1,3+,A)$ of the first 4f–5d transition of Ce^{3+} with that of the $4f^q \rightarrow 4f^{q-1}5d$ transition energies

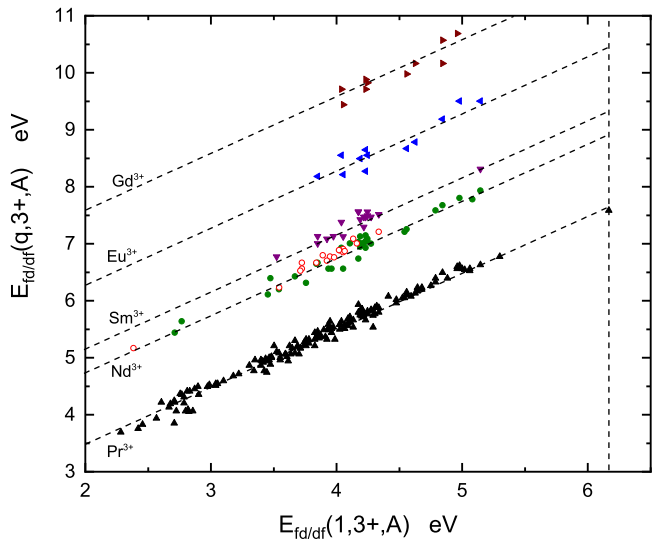

Fig. 10. Lowest energy spin allowed 4f–5d transition energies in the trivalent lanthanides from the left hand branch against that of Ce^{3+}. The open data symbols show the 5d–4f emission to the Nd^{3+} ground state against the 5d–4f emission to the Ce^{3+} ground state.

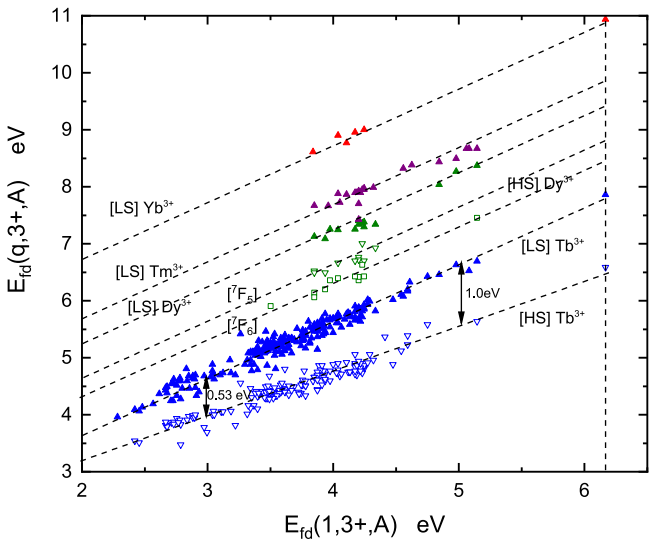

Fig. 11. Lowest energy [HS] spin forbidden and [LS] spin allowed 4f–5d transition energies in the trivalent lanthanides from the right hand branch against that of Ce^{3+}.

Table 5
The energy difference $\Delta E_{fd}^{abs,SA}(q,1,3+)$ averaged over N^{abs} compounds between the first spin allowed 4f–5d absorption in Ln^{3+} with $4f^q$ ground state with that in Ce^{3+} ($q = 1$) and similar for the spin allowed 5d–4f emission to the $4f^q$ ground state.

q	Ln	$\Delta E_{fd}^{abs,SA}(q,1,3+)$	N^{abs}	$\Delta E_{df}^{em,SA}(q,1,3+)$	N^{em}	$E_{fd}^{SA}(q,3+)$
1	Ce	0	780	0	813	6.17
2	Pr	1.51	163	1.52	106	7.68
3	Nd	2.76	33	2.84	18	8.95
4	Pm	–	0	–	0	9.26
5	Sm	3.23	18	3.28	3	9.40
6	Eu	4.30	12	–	0	10.46
7	Gd	5.55	10	5.71	5	11.77
8	Tb	1.64	221	–	0	7.81
9	Dy	3.17	14	–	0	9.33
10	Ho	3.86	11	3.77	2	10.02
11	Er	3.76	21	3.76	7	9.92
12	Tm	3.68	21	3.65	5	9.84
13	Yb	4.77	6	–	0	10.93
14	Lu	6.09	5	6.05	4	12.24

$E_{fd}(q,3+,A)$ of other trivalent lanthanides when on the same site in the same compound [4], and the same for the 5d–4f emission energies. Those energy differences appear to first approximation compound independent. Over the years more and more data have become available that can be used to further improve the values for those constant energy differences. Particularly there are new data on Sm [55–59], Eu [57,60–62], Gd [57,63,64], Yb^{3+} [65,66], and Lu^{3+} [64,67–69] from vacuum ultra violet spectroscopy. Fig. 10 shows the energy for the first spin allowed 4f–5d transition in the lanthanides Pr, Nd, Sm, Eu, and Gd from the left hand branch against that of Ce^{3+}. For practical reasons we will always deal with the energy at the maximum of the side band and not at the zero-phonon line. All data for the spin allowed transitions scatter around straight lines of unit slope. It implies constant energy differences $\Delta E_{fd}^{abs,SA}(q,1,3+)$ between Ln^{3+} with $q = q$ and Ce^{3+} with $q = 1$, and these differences are compiled in column 3 of Table 5 together with the number of compounds information was retrieved from.

Fig. 11 shows 4f–5d transition data for several of the trivalent lanthanides from the right hand branch. Data for the still missing lanthanides can be found in Fig. S2 and Fig. S3 of [Suppl. Info.]. Data are most abundant for Tb^{3+} that usually shows the excitation bands in the well-accessible UV spectral region. Two sets of data are distinguished, that of the first spin allowed Tb^{3+} [LS] transition scatter around a line of unit slope, but that for the lower energy spin forbidden Tb^{3+} [HS] transition scatter around a line with smaller slope of 0.78. For the other lanthanides like Dy, Ho, Er, Tm, Yb, and Lu the available data are all from wide band gap compounds and data fall in the 6–9 eV region. In the case of Dy^{3+} one may observe two [HS] transitions, i.e., those to the $4f^8[^7F_6]5d_1$ and $4f^8[^7F_5]5d_1$ levels. They both appear at lower energy than the first [LS] $4f^8[^7F_6]5d_1$ spin allowed transition. Information from [4,62,66,70–73] was used, and the average energy separation between the two [HS] transitions in Fig. 11 appears to be 0.33 eV (2660 cm^{-1}). This is somewhat larger than the 2200 cm^{-1} between the $4f^8[^7F_6]$ and $4f^8[^7F_5]$ levels of Tb^{3+} because the $4f^8$ electrons of the $4f^85d$ excited states of Dy^{3+} interact with a higher nuclear charge than in Tb^{3+} and hence larger spin–orbit interaction.

Columns 5 and 6 of Table 5 compile data derived from the spin allowed 5d–4f emission energies as gathered for Nd^{3+} in Fig. 10, for Ho^{3+} in Fig. S3 and the other lanthanides in Fig. S4 of [Suppl. Info.]. The energy of 5d–4f emission to the ground state of Nd^{3+} is shown against the energy of 5d–4f emission to the ground state of Ce^{3+} by the open symbols in Fig. 10. They follow the same line of unit slope as the absorption data. This is because the Stokes shift between absorption and emission due to lattice relaxation for both lanthanides Ce and Nd is about the same. For other lanthanides the same is observed [4]. The last column of Table 5 compiles the quasi free ion $E_{fd}^{SA}(q,3+)$ values which are also compiled in Table 2, and that can be used to construct the $4f^{q-1}5d$ level locations in diagrams like Fig. 1. They are obtained from

$$E_{fd}^{SA}(q,3+) = 6.167 + \frac{\Delta E_{fd}^{abs,SA}(q,1,3+)N^{abs} + \Delta E_{df}^{em,SA}(q,1,3+)N^{em}}{N^{abs} + N^{em}} \quad (5)$$

where the constant energy differences in spin allowed absorption and emission are added as a weighted average to the free ion Ce^{3+} 4f–5d energy of 6.167 eV. The listed value of 9.26 eV for Pm^{3+} in Table 5 with $q = 4$ is a conveniently chosen value such that the VRBE in the lowest 5d-state from Nd^{3+} to Sm^{3+}, like in the VRBE schemes in Figs. 1 and 2, shows a smooth progression.

For the lanthanides with $q > 7$ one may also observe the spin forbidden 4f–5d absorption and 5d–4f emissions. Data for the SF absorption in Tb^{3+} and Dy^{3+} are already in Fig. 11. That for Tm, Er, Yb, and Lu are gathered in Fig. S2 of [Suppl. Info.] and for Ho in Fig. S3 of [Suppl. Info.]. Data on SF 5d–4f emission can be found for Ho^{3+} in Fig. S3, and for Lu, Er, and Tm in Fig. S5 of [Suppl. Info.]. With Eq. (5) but then applied to the data on the SF transitions, the result in Table I of [Suppl. Info.] are obtained.

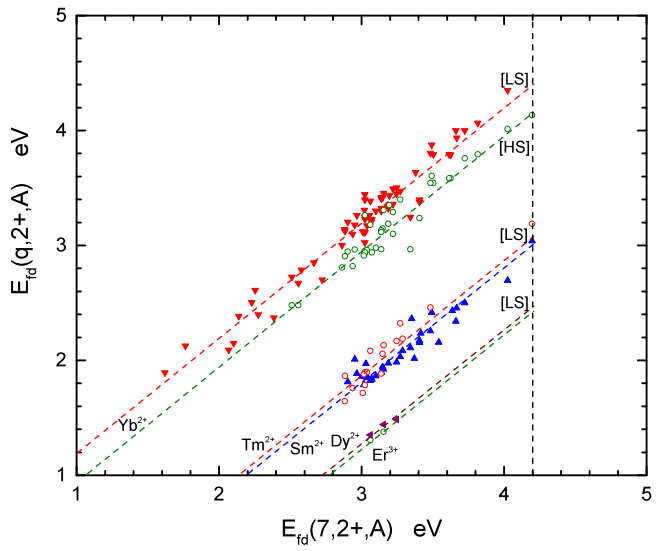

Fig. 12. Energy of the first spin allowed $4f^q \rightarrow 4f^{q-1}5d$ transition of Yb^{2+}, Tm^{2+}, Sm^{2+}, Er^{2+} and Dy^{2+} against that of Eu^{2+}. For Yb^{2+} also data on the spin forbidden transition to the first [HS] state is shown.

Table 6
The energy difference $\Delta E_{fd}^{absSA}(q,7,2+)$ averaged over N^{abs} compounds between the first spin allowed 4f–5d absorption in Ln^{2+} with $4f^q$ ground state configuration with that in Eu^{2+} ($q = 7$) and similar for the spin allowed 5d–4f emission to the $4f^q$ ground state.

q	Ln	$\Delta E_{fd}^{absSA}(q,7,2+)$	N^{abs}	$\Delta E_{df}^{emSA}(q,7,2+)$	N^{em}	$E_{fd}^{SA}(q,2+)$
1	La	−5.09	1	–	0	−0.89
2	Ce	−3.79	1	–	0	0.41
3	Pr	−2.61	1	–	0	1.59
4	Nd	−2.30	1	–	0	1.90
5	Pm					1.94
6	Sm	−1.20	36	−1.19	51	3.00
7	Eu	0	500	0	628	4.20
8	Gd	−3.28	1	–	0	0.6
9	Tb	−2.27	1	–	0	1.85
10	Dy	−1.73	3	–	0	2.55
11	Ho	−1.71	2	–	0	2.49
12	Er	−1.77	2	–	0	2.35
13	Tm	−1.11	17	−1.19	2	3.08
14	Yb	0.20	67	0.14	23	4.38

3.2. The parameters to construct the 5d level locations for divalent lanthanides

A review on the 4f–5d transition energies was made in 2003 for the divalent lanthanides [5], and since then more data have become available. Fig. 12 compiles results on the energy of the first spin allowed 4f–5d transitions in the divalent lanthanides Yb, Sm, Tm, Er, and Dy against that of Eu^{2+}. Like for the trivalent lanthanides, data scatter around lines of unit slope which implies constant energy difference $\Delta E_{fd}^{absSA}(q,7,2+)$ with that of the reference lanthanide Eu^{2+}. These differences are compiled in column 3 of Table 6. For the divalent lanthanides La, Ce, Pr, Nd, Gd, and Tb, the only information is on the free ions and the values from the 2003 review are compiled. Date derived from spin allowed emission for divalent Sm and Tm as gathered in Fig. S6 [Suppl. Info.] and for divalent Yb as gathered in Fig. S7 [Suppl. Info.] are compiled in columns 5 and 6. No spin allowed emission data are available for the other divalent lanthanides.

The last column of Table 6 are the quasi free $E_{fd}^{SA}(q,2+)$ values which are also compiled in Table 1 that can now be used to construct the $4f^{q-1}5d$ level locations for the divalent lanthanides in diagrams like Fig. 1. They are obtained from

$$E_{fd}^{SA}(q,2+) = 4.198 + \frac{\Delta E_{fd}^{absSA}(q,7,2+)N^{abs} + \Delta E_{df}^{emSA}(q,7,2+)N^{em}}{N^{abs} + N^{em}} \quad (6)$$

where Eu^{2+} with $E_{fd}(7,2+,\text{vacuum}) = 4.198$ eV is now the lanthanide of reference.

For Dy, Ho, and Er only 2 or 3 data points are available. We took the liberty to choose a less than 0.1 eV different value for $E_{fd}^{SA}(q,2+)$ than obtained with Eq. (6) which is then the value compiled in Table 6. This was done in order to obtain a smooth progression of the 5d binding energy curve in VRBE schemes. For $q = 1$, 2, 3, 4, and 7 the experimentally known free ion values $E_{fd}^{SA}(q,2+,\text{vacuum})$ that were already discussed in [5] are used. The value of 1.94 eV for Pm^{2+} with $q = 5$ was chosen such that the VRBE in the lowest 5d-state from Nd^{2+} to Sm^{2+} shows a smooth progression in VRBE schemes as for YPO_4 and $La_2Hf_2O_7$. Then we still need to motivate the listed values for Gd^{2+} and Tb^{2+} to complete Tables 1 and 6. That motivation can be found in [Suppl. Info.].

Fig. 12 shows also data on the first [HS] spin forbidden 4f–5d transition for Yb^{2+} and similar can be found for Tm^{2+} in Fig. S6 of [Suppl. Info.]. Data on the spin forbidden emissions in divalent Tm and Yb are gathered in Fig. S6 and Fig. S7 of [Suppl. Info.]. Eq. (6) has been applied to the data on the SF transitions and results can be found in Table II of [Suppl. Info.].

4. Discussion

4.1. The q dependence of the redshift

The vertical dashed lines in Figs. 10 and 11 are drawn at the free ion 4f–5d transition energy $E_{fd}(1,3+,\text{vacuum}) = 6.167$ eV for Ce^{3+}, and in Fig. 12 at the free ion 4f–5d transition energy $E_{fd}(7,2+,\text{vacuum}) = 4.198$ eV for Eu^{2+}. The intercepts with the least squares fitted lines with slope unity then provide the quasi free 4f–5d energies $E_{fd}^{SA}(q,Q)$ for each lanthanide that are listed in Tables 1 and 2. The energy difference between the quasi free ion 4f–5d energy and the observed 4f–5d energy for the lanthanide in a compound is then defined [4,31] as the redshift $D(q,Q,A)$ for that lanthanide in that compound

$$D(q,Q,A) = E_{fd}^{SA}(q,Q) - E_{fd}(q,Q,A). \quad (7)$$

When data scatter around dashed lines of unit slope it implies that the redshift is in first approximation independent on q. This appears to be so for the SA 4f–5d transitions of all lanthanides. One may then write $D^{SA}(q,3+,A) \approx D(1,3+,A)$ and $D^{SA}(q,2+,A) \approx D(7,2+,A)$. The plenty of data available on 4f–5d transitions for Ce^{3+} (see Table 5) and Eu^{2+} (see Table 6) in compounds can then be used to predict the same for all other lanthanides in those compounds. In [30] it was shown, however, that the difference in redshift for Ce^{3+} with that for the SA transition in Tb^{3+} is not random but correlates with the size of the crystal field splitting of the 5d-states. The reason is that the crystal field splitting at a specific site tends to reduce with smaller size of the lanthanide. It may, depending on the size of the crystal field splitting, lead to ± 0.2 eV difference in redshift values. This means that the scattering of data around the dashed lines with unit slope cannot be fully attributed to experimental uncertainties but also has a physical relevance.

The transitions to the ^9D_J and ^7D_J levels for the free ion Tb^{3+} in Fig. 9 are, when in a compound, not observed as a set of individual sharp transitions to each J-state, but instead as a band with its maximum close to the barycenter energy. The barycenter difference $\Delta E^{exc}(8,3+,vacuum)$ for free ion Tb^{3+} is 1.27 eV and for Gd^{2+} $\Delta E^{exc}(8,2+,vacuum) = 1.07$ eV. In compounds this exchange splitting is reduced which can be seen for Tb^{3+} in Fig. 11. It is ≈0.53 eV for compounds with $E_{fd}(1,3+,A)$ ≈3 eV and increases towards ≈1.0 eV for fluorides with $E_{fd}(1,3+,A)$ ≈5 eV. One then expects that [LS] data in diagrams like Figs. 10 and 11 should fall along a line with slope larger than unity and the [HS] data in Fig. 11 along a line with slope smaller than unity. Using values for $\Delta E^{exc}(q,3+,vacuum)$ as presented in [30] and the experimental data for $\Delta E^{exc}(8,3+,A)$, slopes of 0.98, 0.96, and 0.90 for the [HS] data of Pr^{3+}, Nd^{3+}, and Tb^{3+} are predicted, and 1.13 for the [LS] data of Tb^{3+}. The limited range and scatter in the

data for Pr^{3+} and Nd^{3+} do not permit to determine slopes with better than ±0.04 accuracy and the prediction cannot be tested. The [HS] and [LS] data for Tb^{3+} ($q = 8$) in Fig. 11 follow lines with slopes of 0.78 and 1.00 and these are significantly smaller than predicted. An explanation for the 0.12 to 0.13 smaller slopes can be offered by considering the nephelauxetic effect.

When the nephelauxetic effect increases and $\beta(3+,A)$ decreases, the entire right hand branch ($q = 8-14$) of the $4f^q$ curve lowers in energy as illustrated in Fig. 8. In the excitation from $4f^q$ to $4f^{q-1}5d$, a similar nephelauxetic lowering will apply to the $4f^{q-1}$ part of the excited state configuration. When both $4f^q$ ground and $4f^{q-1}5d$ excited states are lowered, the $4f^q$-$4f^{q-1}5d$ energy differences for the [LS] and [HS] states are not much affected by the nephelauxetic effect. This holds for all lanthanides except Tb^{3+} with $q = 8$. We still have the nephelauxetic lowering of the $4f^8$ initial state. However, the $4f^7$ part of the $4f^75d$ final state will be subject to a much smaller nephelauxetic lowering because the $4f^7$ configuration belongs to the left hand branch! The nephelauxetic effect will then augment $E_{fd}(8,3+,A)$ which translates to reduced slopes in the Tb^{3+} [LS] and [HS] data of Fig. 11. Let us compare the class of fluoride compounds with $\beta = 0.96$ and $E_{fd}(1,3+,A) = 5$ eV and the class of compounds with $\beta = 0.92$ and $E_{fd}(1,3+,A) = 5$ eV. By using $S(8,3+) = 6.422$ eV and $S(7,3+) = 0.402$ eV, the nephelauxetic lowering of the $4f^8$ and $4f^75d$ states of Tb^{3+} are obtained for the different classes of compounds. Translated to Fig. 11 it decreases the slope of the lines through both the [HS] and [LS] Tb^{3+} data by an amount of 0.12 which is precisely the additional amount needed to explain the observed slopes of 0.78 and 1.00. The predicted 0.13 increase in the slope due to reduction of exchange splitting is therefore canceled by the 0.12 reduction from the nephelauxetic effect leading to the fortuitous outcome that the Tb^{3+} [LS] data follow a line of unit slope in Fig. 11.

Using the quasi free ion 4f–5d energy $E_{fd}^{SA}(q,Q)$ in the definition of the redshift in Eq. (7) rather than the real free ion energy $E_{fd}(q,Q,\text{vacuum})$ has several practical advantages. Any q dependent part of the redshift that does not depend on type of compound can then be consumed in $E_{fd}^{SA}(q,Q)$. For example, due to the lanthanide contraction, the size of the crystal field splitting reduces along the series which leads to a q dependence. The compound averaged reduction is then consumed in $E_{fd}^{SA}(q,Q)$. In determining $E_{fd}(q,Q,n)$ always the maxima of the broad side bands in absorption or excitation spectra are used and not the zero-phonon lines. Besides, closely spaced multiplets like the ^9D_J states of the $4f^75d$ configurations in Fig. 9 cannot be distinguished and then $E_{fd}(q,Q,A)$ will refer to a barycenter energy. These are q-dependent (lanthanide specific) but compound independent contributions to $E_{fd}(q,Q,A)$ and the redshift. By using $E_{fd}^{SA}(q,Q)$, parts of the q-dependent contributions to $D(q,Q,A)$ are removed, and for many practical purposes one may use $D(2+,A) = D(7,2+,A)$ and $D(3+,A) = D(1,3+,A)$.

In conclusion, for all spin allowed 4f–5d transitions which are those to the [HS] states for $q \le 7$ and to the [LS] states for $q \ge 8$ one may use $E_{fd}^{SA}(q,Q,A) = E_{fd}^{SA}(q,Q) - D(Q,A)$. The method introduced in [3] for the redshift of the [HS] states for $q \ge 8$ as expressed by Eq. (8) can still be used

$$E_{fd}^{HS}(q \ge 8,Q,A) = E_{fd}^{LS}(q \ge 8,Q,A) - \Delta E^{exc}(q,Q)\frac{\Delta E^{exc}(8,3+,A)}{\Delta E^{exc}(8,3+,Ref)} \quad (8)$$

where $\Delta E^{exc}(q,Q)$ are a set of parameters that pertain to the exchange splitting in a reference compound where $\Delta E^{exc}(8,3+,Ref) = 1$ eV which is the typical value for Tb^{3+} in fluoride compounds; then by definition $\Delta E^{exc}(8,3+) = 1$ eV. It is therefore assumed that in a compound the relative change in exchange splitting for all trivalent lanthanides is the same as that for Tb^{3+}. When we also assume that the relative change is the same for divalent lanthanides, Eq. (8) applies both for $Q = 2+$ and $Q = 3+$ but then with other values for $\Delta E^{exc}(q,Q)$. The values for $\Delta E^{exc}(q,Q)$ as derived or otherwise estimated from the results in Table I and Table II of [Suppl. Info.] are compiled in Tables 1 and 2.

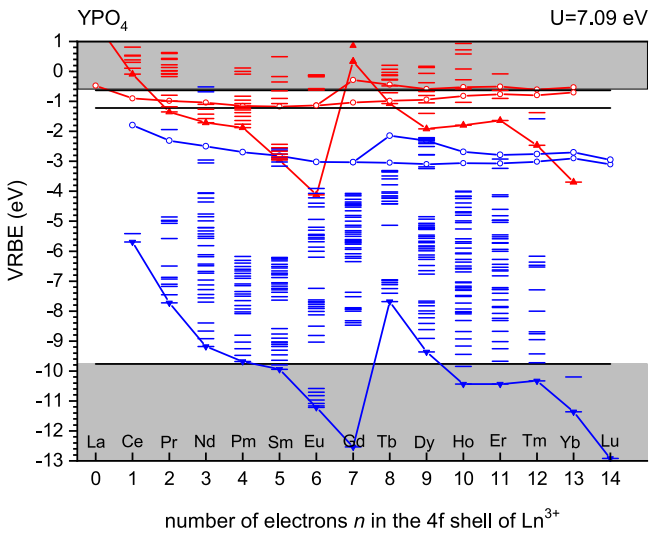

Fig. 13. The vacuum referred binding energy scheme with the lanthanide levels in YPO_4 constructed with the revised method and revised parameters of this work.

4.2. Combining 4f and 5d levels

With Table 1, Table 2, and Eq. (1), we have derived the shape of the lanthanide $4f^q$ zigzag curves and how that changes with the nephelauxetic ratio $\beta(Q,A)$ as shown in Figs. 5 and 8. Here we wish to add the information on the 4f–5d transition energies $E_{fd}(q,Q,A)$ using Eq. (7) and (8) with the experimental compound dependent parameters $D(Q,A)$ and $\Delta E^{exc}(8,3+,A)$ for Tb^{3+}, and the compound independent parameters $\Delta E^{exc}(q,Q)$ listed in Tables 1 and 2. To do so we will regard YPO_4 and $La_2Hf_2O_7$ as our model compounds.

For YPO_4 we used $\beta(3+,A) = 0.94$, $\beta(2+,A) = 0.95$, $\Delta E^{exc}(8,3+,A) = 0.90$ eV, $D(3+,A) = 2.22$ eV, and $D(2+,A) = 1.23$ eV to define all level energies with respect to that of the Eu^{2+} and Eu^{3+} ground state energies. In order to place the Eu^{2+} and Eu^{3+} levels with respect to the valence band top $E_V(A)$ and conduction band bottom $E_C(A)$ and with respect to the vacuum level we also need the energy $E^{ex}(A) = 8.55$ eV of exciton creation, the energy $E^{CT}(6,3+,A) = 5.65$ eV of the Eu^{3+} CT-band, and the parameter $U(6,A) = 7.09$ eV of the chemical shift model as additional compound dependent parameters. The energy at the conduction band bottom is then given by

$$E_C(A) = E_V(A) + E^{ex}(A) + 0.008(E^{ex}(A))^2 \quad (9)$$

where the last term is an estimator for the electron–hole binding energy in the exciton state as proposed in [27].

By using $\alpha(3+) = 0.098$eV/pm and $\alpha(2+) = 0.095$ eV/pm with the ionic radii for the divalent and trivalent lanthanides from Tables 1 and 2 and the nephelauxetic ratios $\beta(Q,A)$ in Eq. (1), the VRBE in the ground states for all divalent and all trivalent lanthanides are obtained. Fig. 13 shows the results for YPO_4. Here we also added the $4f^q$ excited states from the Dieke diagram. The $4f^q$ excited state energies also depend on $\beta(Q,A)$ but that dependence is very small and will be ignored in VRBE diagrams.

Comparing the new VRBE scheme with that of Fig. 1 there are several differences. The right hand branch of the trivalent lanthanide zigzag curve is lowered and it is deeper in the valence band. The VRBE for Tb^{3+} is now at about the same energy as the VRBE of Pr^{3+}. The VRBE in the Ce^{3+} ground state has raised by 0.28 eV. The lowest energy [HS] 5d states for the trivalent lanthanides display a smoother variation with q because of an improved value for $\Delta E^{exc}(9,3+)$ for Dy^{3+} in Table 2. The energy for the Lu^{3+} $4f^{13}5d$ level does not follow the regular trend. It may suggest that parameters for Lu^{3+} are not yet correct. The [LS] and [HS] $4f^{q-1}5d$ right hand branches for the divalent

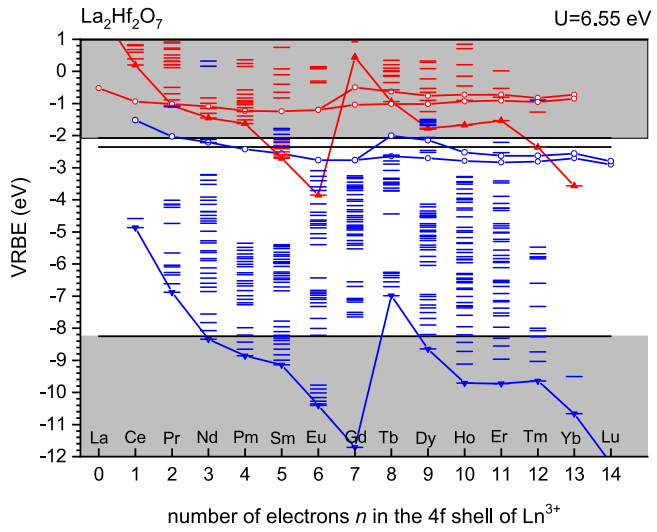

Fig. 14. The vacuum referred binding energy scheme for the divalent and trivalent lanthanide ground state levels in $La_2Hf_2O_7$ constructed with the revised method and revised parameters of this work.

lanthanides are also shown in the new VRBE scheme. Note that they still display few 0.1 eV deviations from a smooth curve which may suggests experimental errors in the used parameters.

Fig. 14 shows the VRBE scheme for $La_2Hf_2O_7$ constructed with $\beta(3+,A) = \beta(2+,A) = 0.92$, $\Delta E_{ex}(8,3+,A) = 0.655$ eV, $D(1,3+,A) = 2.78$ eV, $D(7,2+,A) = 1.54$ eV, $E^{ex}(A) = 5.9$ eV, $E^{CT}(6,3+,A) = 4.4$ eV, $U(6,A) = 6.55$ eV. Comparing with Fig. 2 one observes that the upward jump of the right hand branch [HS] 5d levels has disappeared because both the right hand $4f^q$ ground state and $4f^{q-1}$ part of the excited state undergo a nephelauxetic lowering. Instead, the right hand branch [LS] levels have moved slightly below the conduction band bottom.

5. Summary and conclusions

Parameters for the shape of the 4f and 5d binding energy curves of divalent and trivalent lanthanides have been improved and they are compiled in Tables 1 and 2. Different from previous methods, the 4f zigzag curves are now directly derived from the 3^{rd} and 4^{th} ionization potentials of the lanthanide atoms by applying a compound independent tilt operation and accounting for the nephelauxetic effect as in Eq. (1). The effect of the nephelauxetic ratio $\beta(Q,A)$ on the left hand branch lanthanides is insignificant but the right hand branch lanthanide energies may lower by as much as 0.5 eV depending on type of compound.

All collected data on the spectroscopy of $4f^q \rightarrow 4f^{q-1}5d$ transitions have been re-analyzed to arrive at a new set of quasi free lanthanide 4f–5d energy parameters $E_{fd}^{SA}(q,Q)$. Together with the redshift $D^{SA}(Q,A)$ and exchange $\Delta E^{exc}(q,Q,A)$ values they provide the [LS] and [HS] $4f^{q-1}5d$ binding energy curves. For many practical applications one may regard the redshift of the first spin allowed 4f–5d transition as a materials property and independent on the type of lanthanide. It was already known that the crystal field splitting of 5d-levels depends on the ionic radius of the lanthanide which leads to a q dependence in the redshift that may amount several 0.1 eV. It explains part of the scattering of data around the lines with unit slope in figures like Fig. 10. It was also known that the reduction of the exchange splitting between spin allowed and spin forbidden 4f–5d transitions introduces a q dependence to the redshift. In this work we have added the nephelauxetic effect as yet another cause of redshift variation. For the spin allowed transition in Tb^{3+} the effect of the reduction of exchange splitting cancels the effect of the nephelauxetic effect, and therewith offered an explanation why the data for the [LS] 4f–5d transitions follow a line of unit slope in Fig. 11. Both effects enhance each other for the [HS] transitions and this provides an explanation why those data follow a line with slope 0.78 in Fig. 10.

Improved VRBE schemes can now be constructed by combining the compound independent parameters of Tables 1 and 2 with in total eight compound dependent parameters. These are $U(6,A)$, $E^{CT}(6,3+,A)$, $E^{ex}(A)$, $\beta(Q,A)$, $D(Q,A)$, and $\Delta E^{exc}(8,3+,A)$. That still may seem a lot, but actually the compound dependent parameter values are strongly correlated to each other, and they show clear trends with changing structural and compositional properties of the compound.

Declaration of competing interest

The authors declare that they have no known competing financial interests or personal relationships that could have appeared to influence the work reported in this paper.

CRediT authorship contribution statement

Pieter Dorenbos: Conceptualization, Writing - review & editing.

Appendix A. Supplementary data

Supplementary material related to this article can be found online at https://doi.org/10.1016/j.jlumin.2020.117164.

References

[1] E. Nakazawa, J. Lumin. 100 (2002) 89.
[2] C. Pedrini, F. Rogemond, D.S. McClure, J. Appl. Phys. 59 (1986) 1196.
[3] P. Dorenbos, ECS J. Solid State Sci. Technol. 2 (2013) R1.
[4] P. Dorenbos, J. Lumin. 91 (2000) 91.
[5] P. Dorenbos, J. Phys.: Condens. Matter. 15 (2003) 575.
[6] P. Dorenbos, Phys. Rev. B 62 (2000) 15640.
[7] P. Dorenbos, Phys. Rev. B 62 (2000) 15650.
[8] P. Dorenbos, Phys. Rev. B 64 (2001) 125117.
[9] P. Dorenbos, J. Lumin. 99 (2002) 283.
[10] P. Dorenbos, Phys. Rev. B 65 (2002) 235110.
[11] P. Dorenbos, J. Phys.: Condens. Matter 15 (2003) 8417.
[12] P. Dorenbos, Phys. Rev. B 85 (2012) 165107.
[13] P. Dorenbos, Phys. Rev. B. 87 (2013) 035118.
[14] M. Stephan, M. Zachau, M. Groting, O. Karplak, V. Eyert, K.C. Mishra, P.C. Schmidt, J. Lumin. 114 (2005) 255.
[15] H. Retot, S. Blahuta, A. Bessiere, B. Viana, B. LaCourse, E. Mattmann, J. Phys. D: Appl. Phys. 44 (2011) 235101.
[16] E.D. Milliken, L.C. Oliveira, G. Denis, E.G. Yukihara, J. Lumin. 132 (2012) 2495.
[17] A. Chaudhry, A. Canning, R. Boutchko, M.J. Weber, N. Gronbech-Jensen, S.E. Derenzo, J. Appl. Phys. 109 (2011) 083708.
[18] Roland Gillen, Stewart J. Clark, John Robertson, Phys. Rev. B 87 (2013) 125116.
[19] D. Wu, M.P. Prange, F. Gao, S. Kerisit, J. Lumin. 176 (2016) 227.
[20] Jun Wen, Lixin Ning, Chang-Kui Duan, Yonghu Chen, Yongfan Zhang, Min Yin, J. Phys. Chem. C 116 (2012) 20513.
[21] Shota Takemura, Kazuyoshi Ogasawara, J. Lumin. 214 (2019) 116542.
[22] G.K. Liu, M.P. Jensen, P.M. Almond, J. Phys. Chem. A 110 (2006) 2081.
[23] Yuntao Wu, Guohao Ren, M. Nikl, D. Ding, J. Wang, S. Shang, F. Yang, S. Pan, J. Phys. Chem. A 115 (2011) 13821.
[24] LiXun Yang, Xin Xu, LuYuan Hao, XiuFang Yang, JiaYe Tan, Opt. Mater. 33 (2011) 1695.
[25] G. Pilania, K.J. McClellan, C.R. Stanek, B.P. Uberuaga, J. Chem. Phys. 148 (2018) 241729.
[26] Jumpei Ueda, Ryomei Maki, Setsuhisa Tanabe, Inorg. Chem. 56 (2017) 10353.
[27] P. Dorenbos, Opt. Mater. 69 (2017) 8.
[28] P. Dorenbos, Opt. Mater. 91 (2019) 333.
[29] P. Dorenbos, J. Lumin. 214 (2019) 116536.
[30] P. Dorenbos, J. Phys.: Condens. Matter 15 (2003) 6249.
[31] P. Dorenbos, J. Lumin. 91 (2000) 155.
[32] P. Dorenbos, J. Lumin. 104 (2003) 239.
[33] C.K. Jørgensen, Mol. Phys. 5 (1962) 271.
[34] C.K. Jørgensen, Modern Aspects of Ligand Field Theory, North-Holland Publishing Company, Amsterdam, 1971.
[35] P. Dorenbos, J. Phys.: Condens. Matter 15 (2003) 2645.
[36] R.D. Shannon, Acta Crystallogr. A 32 (1976) 751.
[37] C.-G. Ma, M.G. Brik, Q.-X. Li, Y. Tian, J. Alloys Compd. 599 (2014) 93.
[38] P. Caro, J. Derouet, Bull. Soc. Chim. Fr. 1 (1972) 46.

[39] Peter A. Tanner, Yau Yuen Yeung, J. Phys. Chem. A 117 (2013) 1072.
[40] A.J.J. Bos, Materials 10 (2017) 1357.
[41] A.J.J. Bos, P. Dorenbos, A.Q. Bessiere, A. Lecointre, M. Bedu, M. Bettinelli, F. Piccinelli, Rad. Meas. 46 (2011) 1410.
[42] A.J.J. Bos, P. Dorenbos, A. Bessiere, B. Viana, Rad. Meas. 43 (2008) 222.
[43] V.A. Arkhangelskaya, M.N. Kiseleva, V.M. Shraiber, Sov. Phys. Solid State USSR 11 (1969) 714 (p.869 in Russian).
[44] E.A. Radzhabov, V.A. Kozlovsky, Rad. Meas. 122 (2019) 63.
[45] P. Dorenbos, J. Phys.: Condens. Matter 25 (2013) 225501.
[46] P. Boutinaud, R. Mahiou, E. Cavalli, M. Bettinelli, J. Appl. Phys. 96 (2004) 4923.
[47] P. Boutinaud, E. Pinel, M. Oubaha, R. Mahiou, E. Cavalli, M. Bettinelli, Opt. Mater. 28 (2006) 9.
[48] P. Boutinaud, P. Putaj, R. Mahiou, E. Cavalli, A. Speghini, Spectrosc. Lett. 40 (2007) 209.
[49] Tianshuai Lyu, Pieter Dorenbos, J. Mater. Chem. C. 6 (2018) 369.
[50] Tianshuai Lyu, Pieter Dorenbos, J. Mater. Chem. C. 6 (2018) 6240.
[51] Tianshuai Lyu, Pieter Dorenbos, Chem. Eng. J. 372 (2019) 978.
[52] Tianshuai Lyu, Pieter Dorenbos, Chem. Eng. J., under review.
[53] Fangtian You, A.J.J. Bos, Qiufeng Shi, Shihua Huang, P. Dorenbos, Phys. Rev. B. 85 (2012) 115101.
[54] Hongde Luo, Adrie J.J. Bos, Pieter Dorenbos, J. Phys. Chem. C 120 (2016) 5916.
[55] E.A. Radzhabov, Opt. Mater. 85 (2018) 127.
[56] P. Solarz, G. Dominiak-Dzik, W. Ryba-Romanowski, J. Alloys Compd. 362 (2004) 61.
[57] P.A. Tanner, C.-K. Duan, V.N. Makhov, M. Kirm, N.M. Khaidukov, J. Phys.: Condens. Matter 21 (2009) 395504.
[58] T. Shalapska, P. Dorenbos, A. Gektin, G. Stryganyuk, A. Voloshinovskii, J. Lumin. 155 (2014) 95.
[59] V.P. Dotsenko, I.V. Berezovskaya, N.P. Efryushina, A.S. Voloshinovskii, G.B. Stryganyuk, J. Mater. Sci. 45 (2010) 1469.
[60] M. Kirm, Y. Chen, S. Neicheva, K. Shimamura, N. Shiran, M. True, S. Vielhauer, Phys. Status Solidi c 2 (2005) 418.
[61] A.H. Krumpel, E. van der Kolk, D. Zeelenberg, A.J.J. Bos, K.W. Krämer, P. Dorenbos, J. Appl. Phys. 104 (2008) 073505.
[62] Chong-Geng Ma, M.G. Brik, W. Ryba-Romanowski, H.C. Swart, M.A. Gusowski, J. Phys. Chem. A 116 (2012) 9158.
[63] V.N. Makhov, S.Kh. Batygov, L.N. Dmitruk, M. Kirm, G. Stryganyuk, G. Zimmerer, Phys. Status Solidi c 4 (2007) 881.
[64] M. Kirm, G. Stryganyuk, S. Vielhauer, G. Zimmerer, V.N. Makhov, B.Z. Malkin, O.V. Solovyev, R. Yu. Abdulsabirov, S.L. Korableva, Phys. Rev. B 75 (2007) 075111.
[65] E. Radzhabov, A. Nepomnyashchikh, Solid State Commun. 146 (2008) 376.
[66] L. van Pieterson, M.F. Reid, G.W. Burdick, A. Meijerink, Phys. Rev. B 65 (2002) 045114.
[67] V.N. Makhov, S.Kh. Batygov, L.N. Dmitruk, M. Kirm, S. Vielhauer, G. Stryganyuk, Phys. Solid State 50 (2008) 1625.
[68] V.N. Makhov, T. Adamberg, M. Kirm, S. Vielhauer, G. Stryganyuk, J. Lumin. 128 (2008) 725.
[69] N.Yu. Kirikova, M. Kirm, J.C. Krupa, V.N. Makhov, E. Negodin, J.Y. Gesland, J. Lumin. 110 (2004) 135.
[70] A.N. Belsky, N.M. Khaidukov, J.C. Krupa, V.N. Makhovd, A. Philippov, J. Lumin. 94–95 (2001) 45.
[71] Jiuping Zhong, Hongbin Liang, Bing Han, Zifeng Tian, Qiang Su, Ye Tao, Opt. Express 16 (2008) 7508.
[72] Bing Han, Hongbin Liang, Huihong Lin, Wanping Chen, Qiang Su, Guangtao Yang, Guobin Zhang, J. Opt. Soc. Amer. B (2008) 2057.
[73] G. Dominiak-Dzik, W. Ryba-Romanowski, L. Kovacs, E. Beregi, Rad. Meas. 38 (2004) 557.